6-2018

Baroclinic Tidal Sea Level from Exact-Repeat Mission Altimetry

Edward Zaron
Portland State University, ezaron@pdx.edu

Baroclinic Tidal Sea Level from Exact-Repeat Mission Altimetry

Edward D. Zaron*

Portland State University, Portland, Oregon

**Corresponding author address:* Department of Civil and Environmental Engineering, Portland State University, P.O. Box 751, Portland, OR 97207-0751, USA

E-mail: ezaron@pdx.edu

ABSTRACT

A near-global model for the sea-surface expression of the baroclinic tide has been developed using exact-repeat mission altimetry. The methodology used differs in detail from other altimetry-based estimates of the open ocean baroclinic tide, but it leads to estimates which are broadly similar to previous results. It may be used for prediction of the baroclinic sea level anomaly at the frequencies of the main diurnal and semidiurnal tides, K_1, O_1, M_2, S_2, as well as the annual modulates of M_2, denoted MA_2 and MB_2. The tidal predictions are validated by computing variance reduction statistics using independent sea-surface height data from the CryoSat-2 altimeter mission. Typical mid-ocean baroclinic tidal signals range from a few millimeters to centimeters of elevation, corresponding to sub-surface isopycnal displacements of 10's of meters; however, in a few regions larger signals are present and it is found that the present model can explain more than 13 cm^2 variance at some sites. The predicted tides are also validated by comparison with a database of hourly currents inferred from drogued surface drifters. The database is large enough to permit assessment of a simple model for scattering of the low-mode tide. Results indicate a scattering time scale of approximately one day, consistent with a priori estimates of time-variable refraction by the mesoscale circulation.

1. Introduction

Satellite altimetry has enriched our understanding of ocean dynamics by providing a sustained and near-global view of mean sea level and mesoscale eddies during the last 25 years (Fu and Cazenave 2001), it is now widely used in ocean forecasting (Willis et al. 2010), and it is contributing to a broad range of research on ocean and climate processes (Lyszkowicz and Bernatowicz 2017). Studies of ocean tides have been invigorated by the unique datasets generated with altimetry, leading to improved tide predictions (Stammer et al. 2014) and quantitative maps of tidal dissipation (Egbert and Ray 2000, 2001).

The astronomical tidal forcing, i.e., the perturbation of near-Earth gravity caused by the Sun and Moon, does not vary significantly over the depth of the ocean (Doodson and Warburg 1941), so the work done on the ocean by the tidal forcing is input almost exclusively to the barotropic tide (Kelly 2016). Significant energy loss from the barotropic tide occurs in shallow water on continental shelves, and in deep water at sea floor topography. In the latter case the tidal flow disturbs isopycnal surfaces and creates baroclinic pressure gradients which propagate as internal waves (Baines 1982). This process of barotropic tidal energy loss, leading to baroclinic tidal generation in the deep ocean, amounts to roughly a 1 TW rate of work (Egbert and Ray 2001, 2003; Egbert et al. 2004). Although the latter barotropic to baroclinic conversion accounts for only 1/3 of the tidal dissipation, the rate of work is similar to that done by wind on the ocean (Scott and Xu 2009), exclusive of the wind-work involved in generating surface waves and stirring the mixed layer. The vertical potential energy flux driven by the dissipation of these energy inputs is connected to the thermohaline circulation, meridional heat flux, and other climatically-relevant transport processes (Wunsch and Ferrari 2004). Once generated, the baroclinic tide can transport energy for 1000's of kilometers, but the locations and mechanisms whereby it dissipates are not known adequately. Ocean circulation climate models are sensitive to the detailed spatial distribution of the dissipation (Melet et al. 2013) so there is ongoing concern with mapping it empirically.

Because tidal periodicities are aliased by satellite sampling, altimetry can only identify that component of the baroclinic tide which is phase locked with the astronomical tidal forcing. Hence, the baroclinic dissipation inferred from altimeter-derived maps is a combination of apparent dissipation due to the loss of coherence of the tide caused by time-variable modulations of the propagation medium (Park and Watts 2006; Rainville and Pinkel 2006), and irreversible dissipation due to processes such as wave-wave interactions (MacKinnon and Winters 2005; Ward and Dewar 2010; Wunsch 2017), shear-driven mixing (St. Laurent and Nash 2004), and wave breaking (Legg and Huijts 2006). The processes just mentioned range from weakly- to strongly-nonlinear, and it is not clear the degree to which they can be distinguished using ocean observations. Likewise, the extent to which turbulent transport resulting from these processes can be localized to the site of energy loss from the baroclinic tide is also not presently understood. The topic of baroclinic energetics is not directly addressed, here; however, the Discussion section indicates how a combination of sea surface height and tidal current observations might address these issues in the future.

The goal of the present work is to construct accurate maps of the baroclinic tide useful for both tidal prediction and for dynamical studies in the open ocean. Because in situ observations of baroclinic tidal currents are typically highly variable, it was a surprise when baroclinic tides were observed with altimetry (Ray and Mitchum 1996; Kantha and Tierney 1997; Ray and Cartwright 2001; Carrère et al. 2004). Although baroclinic tides are associated with subsurface isopycnal displacements up to 100 m (Alford et al. 2010), the baroclinic pressures are equivalent to just a few centimeters of ocean surface elevation, which makes them challenging to measure and reliably map. Nonetheless, some measure of success has been possible using data from long records of multi-mission satellite altimetry and data fitting techniques which range from interpolation with radial basis functions (Ray and Zaron 2016), to plane-wave fitting using theoretically predicted dispersion relations (Zhao et al. 2016), to Kalman filtering in the spatial domain (Dushaw 2015). The motivation to produce accurate baroclinic tidal predictions grows out of the desire to remove aliased tidal variability from a variety of ocean observations (Zaron and Ray 2017), which will be especially important for making use of observations from the anticipated Surface Water & Ocean Topography (SWOT) swath altimeter mission (Gaultier et al. 2016).

The rest of this paper is organized as follows. First, the altimeter data and harmonic analysis are briefly described, emphasizing minor innovations compared to previous approaches in the literature. Then, the spatial model and other details involved in estimating gridded tidal fields are described, along with a brief comparison with independent altimeter data to illustrate the use of the model for prediction of baroclinic tidal sea surface height (SSH). In order to infer energetics from the mapped SSH fields, some model for the tidal dynamics is needed, and this is explored by detailed comparison with a large database of surface currents observed with Lagrangian drifters. Finally, the results are discussed in the context of other studies, and the article concludes with a brief summary.

2. Altimetry Data and Harmonic Analysis

The satellite altimeter data used in the present analysis are listed in Table 1, representing essentially all the exact-repeat altimeter mission data available during the 1992-2017 time period. By far the largest quantity of observations lie along the TOPEX/Jason reference orbit, but the other missions are essential for resolving the spatial structure of the baroclinic tide.

The path delay and geophysical corrections applied to the data are conventional and follow the GDR-D standard (Picot et al. 2012, 2014) with two minor innovations. The first innovation is that the barotropic ocean tide and earth load tide are corrected using the Goddard/Grenoble Ocean Tide model, version 4.10c (GOT4.10c; an updated version of the model developed in Ray 1999), which has been smoothly extrapolated by the author up to the coastline. The second innovation is that an estimate of the mesoscale sea level anomaly (SLA) is also subtracted from the SSH in order to remove as much non-tidal signal as possible, prior to harmonic analysis. The rationale and impact of this correction have been discussed previously (Ray and Byrne 2010; Ray and Zaron 2016), so it shall not be repeated here. As shown in Ray and Zaron (2011), the methodology used to estimate the mesoscale SLA from multi-satellite altimetry (Anonymous 2014; Pujol et al. 2016) does not completely filter out the baroclinic tidal signals. Filtering the baroclinic tidal signals from the mesoscale SLA estimate prior to using it as a correction is necessary, and this procedure is detailed in Zaron and Ray (2018).

Aside from the minor changes just described, the data processing is essentially identical to that used previously for harmonic analysis of along track altimetry. The altimeter data from missions with the same orbit ground tracks are assembled into time series at each point along the nominal ground track. Each time series is then harmonically analyzed using conventional methods (Cherniawsky et al. 2001; Carrère et al. 2004).

Some care is needed when choosing the tidal frequencies for mapping baroclinic tides. The first consideration is whether or not the aliased tidal frequencies can be determined with the given length of record for the given orbits. The second consideration is the extent of overlap or contamination by tidal frequencies which are not part of the analysis.

To address the first consideration, Table 2 lists the aliases and synodic periods for the tides which are mapped below, M_2, S_2, K_1, O_1, and the annual modulates of M_2, denoted MA_2 and MB_2 (Huess and Andersen 2001). The synodic period is the time needed to accumulate a phase difference of 2π between signals at the given alias periods. For missions in the TOPEX/Jason reference orbit, the alias frequencies of these tides are unambiguously separable using time series longer than 3 years. For the Geosat Follow-On mission (G1A) in the Geosat orbit, the M_2, O_1, and MB_2 frequencies can be accurately identified, but the S_2 and K_1 tidal aliases require a 12 year time series to separate, and the MA_2 and S_2 aliases essentially coincide. Thus, the estimates of MA_2, S_2 and K_1 are inaccurate from G1A. The ERS/Envisat orbit is Sun-synchronous, so S_2 cannot be determined by missions in this orbit. There is a near overlap of O_1 and MA_2, so these tides also cannot be determined accurately from these missions.

In order to address the second consideration, it is necessary to inspect the synodic periods of a larger set of tides. This has been done for the set M_2, S_2, N_2, K_2, K_1, O_1, P_1, and Q_1, together with their annual modulates (not shown). For the missions in the TOPEX/Jason orbits, these additional frequency pairs extend the synodic period to about 6 years, which does not lead to problems with the present data sets. For the G1A orbit, the annual modulates of S_2 are found to nearly overlap with M_2, which adds to noise in harmonic constants. Missions in the ERS/Envisat orbit are more problematic; separation of M_2 and its annual modulates from N_2 and its annual modulates requires almost 9 years of data (Andersen 1995), so the baroclinic N_2 tide is a source of noise here. Likewise, the K_1–P_1 pair requires a nodal cycle to separate, so the presence of P_1 signals adds noise to K_1. Overlaps of the tidal aliases and the annual and semi-annual cycles also exist, but fortunately the annual and semi-annual signals in the open ocean are captured by the mesoscale SLA maps, and removed prior to harmonic analysis.

3. Spatial Model and Mapping

Previous efforts to map the baroclinic tides have used a variety of models to describe its spatial structure. For example, Ray and Zaron (2016) simply used an ad-hoc radial basis function to smoothly interpolate harmonic constants between orbit ground tracks, yielding estimates of baroclinic tidal fields with a minimum of assumptions about their dynamics or spatial coherence. The consistency of the results with the predicted wavenumber dispersion relation for linear inertia-gravity waves supports other methodologies in which these dynamics are assumed. The maps of Dushaw (2015) directly use the dispersion relation for internal waves at the tidal frequencies, deriving the spatial coherence from the assumed dynamics. An even more constrained spatial model is the plane-wave fitting used by Zhao et al. (2016), in which the spatial fields are assumed to be comprised of small number of waves propagating in directions inferred from the data.

Experience with the plane-wave fitting indicates that the baroclinic tidal fields closely obey linear dynamics (Ray and Cartwright 2001; Zhao et al. 2012; Zhao 2016); however, there is a tradeoff between bias and stability which depends on the complexity of the spatial model. For example, both empirical estimates and numerical models of baroclinic tides find a great deal of spatial structure and anisotropy, with waves organized into relatively narrow beams as the result of distributed sources and wave interference (Rainville et al. 2010). The unstructured signal model of Ray and Zaron (2016) is biased towards zero far from the data sites, and it is found that simply increasing the harmonic constants by 5% to 20%, depending on location, improves the accuracy of the tidal predictions made with the model. Similarly, one would expect the highly-structured plane-wave model of Zhao et al. (2016) to be biased in a wave field composed of relatively narrow beams. The bias depends on the size of the fitting window, but one would expect it to be proportional to $\partial^2\eta/\partial y^2$, where η is baroclinic tidal amplitude and y is a coordinate perpendicular to the local propagation direction.

Based on the above, a spatial model was hypothesized which represents the baroclinic wave field locally with a small number of propagating waves combined with a polynomial amplitude modulation. To make these ideas precise, let $\mathbf{x} = (x, y)$ represent Cartesian coordinates on a locally-defined tangent plane, and assume that the baroclinic tide can be represented with N spatially-modulated plane waves, each with wavenumber modulus k_n and direction ϕ_n, for $n = 1, \ldots, N$.

Assuming the amplitude envelope is modulated by a polynomial of order P, then the local spatial signal model for the complex amplitude of the baroclinic tide, η, is given by,

$$\eta(x,y) = \sum_{n=1}^{N} \sum_{p=0}^{P} \sum_{q=0}^{P-p} x^p y^q \left(a_{pqn} \cos(\mathbf{k}_n \cdot \mathbf{x}) + b_{pqn} \sin(\mathbf{k}_n \cdot \mathbf{x}) \right), \tag{1}$$

where vector wavenumber is given by $\mathbf{k}_n = k_n(\cos\phi_n, \sin\phi_n)$, and complex coefficients (a_{pqn}, b_{pqn}) are found by weighted least-squares fitting to the harmonically analyzed altimeter data. With this representation, the component of the wave field propagating parallel to $\mathbf{k_n}$ is given by,

$$\eta_+(x,y) = \frac{1}{2} \sum_{n=1}^{N} \sum_{p=0}^{P} \sum_{q=0}^{P-p} x^p y^q (a_{pqn} - i b_{pqn}) \left(\cos(\mathbf{k}_n \cdot \mathbf{x}) + i \sin(\mathbf{k}_n \cdot \mathbf{x}) \right), \tag{2}$$

and the anti-parallel component is given by,

$$\eta_-(x,y) = \frac{1}{2} \sum_{n=1}^{N} \sum_{p=0}^{P} \sum_{q=0}^{P-p} x^p y^q (a_{pqn} + i b_{pqn}) \left(\cos(\mathbf{k}_n \cdot \mathbf{x}) - i \sin(\mathbf{k}_n \cdot \mathbf{x}) \right). \tag{3}$$

Note that η and the model parameters, $(k_n, \phi_n, a_{pqn}, b_{pqn})$, are together a function of tidal frequency, $\omega \in \{\omega_{\mathrm{M}_2}, \ldots\}$. When it is necessary to indicate this dependence it will be shown using superscript notation, e.g., $\eta^{(\mathrm{M}_2)}(x,y)$ is the complex amplitude of the M_2 harmonic constant.

It remains to be stated how P, N, k_n, and ϕ_n are determined. The procedure is explained here, but the reader may wish to note Figure 1, which indicates the regions illustrated in detail in Figures 2-4 referred to below. The order of the polynomial is simply chosen as $P = 2$, which eliminates the leading-order bias term of a plane-wave fit. Determining N, the number of component waves, is done with a preliminary analysis in which k_n and ϕ_n are determined through an incremental model-building exercise. The procedure is as follows. The empirical along-track harmonic constants, $\eta_o(x_i, y_j)$, are assembled in locally-defined coordinates, $-L/2 \leq x_i \leq L/2$ and $-L/2 \leq y_i \leq L/2$, where L is the size of the two-dimensional data fitting window. Within the fitting window the harmonic constants are placed in square bins of size Δx, averaging data from crossing tracks if necessary. The data within the grid are then regarded as the field of harmonic constants multiplied by the spatial sampling pattern of the altimeter ground tracks (Figure 2a). The contents of this array are windowed (Figure 2b) and the two-dimensional Fourier transform is taken. In essence, the resulting two-dimensional spectrum is the convolution of the baroclinic tide SSH with the antenna pattern of the ground tracks (Fig. 2c). In spite of the modulation by the antenna pattern, peaks in the spectrum are clearly identifiable (Fig. 2d). The two-dimensional spectrum is integrated azimuthally and the peak wavenumber used to assign k_n (Fig. 2g). Then, the two-dimensional spectrum is integrated radially from $(3/4)k_n$ to $(4/3)k_n$ and the azimuthal direction of the peak is assigned to ϕ_n (Fig. 2j). A simple plane-wave fit is computed and subtracted from the data, and the process is repeated until an insignificant amount of variance is removed.

It is useful to examine examples of this procedure in different regions, and this is shown in Figures 2-4 for three very different sites in the Pacific. Figure 2 is from a region northeast of the Hawaiian Ridge where the wave field is dominated by a northbound mode-1 wave from the Ridge and a southbound wave from the Aleutians. The power spectrum of the windowed data (Fig. 2d) clearly shows the peaks associated with the northward and southward propagating beams, with the expected wavelength (170 km; Fig. 2g) and propagation directions (about $\pm 70°$ from east; Fig. 2j). When the first wave is removed, the spectrum of the residual is dominated by the southward wave (Fig. 2e, h, and k). The splitting of the northward peak after the first and second waves are removed (Fig. 2e and f) indicates that it is not well-represented by a simple plane wave. Based on the shape of the spectral peak, it appears to be better represented by a radially-spreading wave (Fig. 2d); however, this spatial model is not part of this preliminary exercise which is only intended to identify (k_n, ϕ_n). The units of the integrated spectra in the last two rows, $\mathrm{mm}^2/\mathrm{cpk}$ and $\mathrm{mm}^2/\mathrm{rad}$, allow the results to be compared with the data in the following two figures. Note that the two-dimensional spectra in the second row are log-scaled, showing three orders of magnitude, and the colors are normalized by the maximum value. Thus, as the residual gets smaller, the peaks stand out less above the noise floor (Fig. 2f, i, l).

The wave field in the Subtropical Western Pacific is primarily composed of three mode-1 waves (Fig. 3a, b, and d), and the amplitudes of these waves (Fig. 3g, h, and i) are larger than those described above near the Hawaiian Ridge. Note also that the noise floor of the radial wavenumber spectrum (e.g., Fig. 3i) is noticeably elevated compared to the previous case (Fig. 2i). Presumably this is related to the higher level of mesoscale kinetic energy in this region.

The wave field in the Equatorial Pacific is much more directional than the previous examples (Fig. 4a, b, d). The wave fitting identifies two mode-1 waves and one mode-2 wave, all propagating to the south. Once again, notice how fitting with a single plane wave changes the directional distribution of variance (Fig. 4j vs. Fig. 4k), suggesting that radial spreading is significant even within these small analysis windows.

The antenna patterns are generally similar in these examples since they primarily depend on the ground track spacing among the missions (Figs. 2-4, panel c). Note that the Nyquist wavenumber, approximately 0.08 cpk, lies far outside the displayed range of wavenumbers. In fact, the antenna patterns are increasingly structured at large wavenumbers because of the high-wavenumbers associated with the across-track sampling. Fortunately, the tidal fields contain so little variance at these small spatial scales that the leakage is not problematic for low wavenumbers, $|\mathbf{k}| < 25 \times 10^{-3}$ cpk.

Table 3 lists the parameters for the spatial models for each of the tides considered. The analysis window of M_2, $L = 500$ km, is smaller than that used for the other tides. A larger window, $L = 1000$ km, is used for S_2, MA_2, and MB_2 because the along-track estimates of these tides are less accurate than M_2, as discussed in Section 2. The larger window, $L = 1000$ km, is used for the K_1 and O_1 tides in order to resolve the longer wavelength of these diurnal tides compared to the M_2 tide. Although the window is of size L, parameters in the model are determined by fitting the data with a weighting function, $\exp(-(5|\mathbf{x}|/L)^2))$, so essentially just data from the middle third of the analysis window are used. As mentioned in the caption of Table 3, this function is also used to window the data prior to computing the two-dimensional power spectrum for determination of (k_n, ϕ_n)

The procedure just described leads to a sequence of estimates for the dominant wavenumbers, modulus and direction (k_n, ϕ_n), for $n = 1, \ldots, N$, ordered according to the variance explained in the 2-dimensional wavenumber domain. But how should the size of this expansion, N, be determined? Experimentation with the F-test, in which the ratio of explained-to-prior variance is compared to that expected by chance (Jenkins and Watts 1968), and Aikake's Information Criterion (Bozdogan 1987) found that both methods sometimes lead to spurious results, apparently due to occasional outliers. Instead, a simpler criterion was used. Namely, the expansion was truncated at $n = N$ when the $n = N + 1$ wave removed less than 1.5 mm^2 variance. The numeric value here was chosen to be approximately equal to the formal error estimate of the harmonic constants from the longest merged time series (TXA, J1A, J2A, J3A; Table 1). The value of N, which is typically in the range of 2 to 5 waves, is thus based on a subjective criterion designed to avoid over-fitting the observations.

With the spatial model defined as above, the mapping proceeds by dividing the ocean into patches of size $L \times L$ in a local tangent plane centered on latitude and longitude coordinates (λ_k, θ_l). The patches lie on a regular overlapping grid of latitudes, $\Delta\theta = \theta_{l+1} - \theta_l$, such that $2\pi r_e \Delta\theta = r_{ol} L$, where r_e is the mean radius of the Earth and $r_{ol} = 1/4$ determines the extent of overlap. The longitude grid is also equidistant between the local tangent planes, $\Delta\lambda = \lambda_{k+1} - \lambda_k$, where $2\pi r_e \cos(\theta_l)\Delta\lambda = r_{ol} L$; note that $\Delta\lambda$ and λ_k depend on l, but this dependence is suppressed in the notation for readability.

Previous published maps of the baroclinic tides have utilized along-track high-pass filtering of the data in order to suppress errors at wavelengths longer than 500 km, but this leads to a non-isotropic antenna response and filtering of east-west propagating waves (Ray and Zaron 2016). To overcome this problem, the present approach estimates the model parameters by fitting the along-track sea surface slope, rather than SSH. This reduces the influence of long-wavelength errors in the data, but because the same operation is applied to both the input data and the signal model, there is no loss of sensitivity to wavenumbers oriented in the east-west directions.

Finally, the complex coefficients (a_{pqn}, b_{pqn}) in equation (1) are determined by conventional weighted least-squares within each analysis window. The weights used are the inverse of the squared standard error estimates from the along-track harmonic analysis (Cherniawsky et al. 2001).

Once the model coefficients are found for each patch, the estimated tidal fields are gridded on a regular latitude-longitude grid at a resolution of $\Delta\Theta = (1/20)^{\circ}$ by weighted averaging of the overlapping patches. The averaging kernel is a radial basis function, $\exp(-(|\mathbf{x}-\mathbf{x_{kl}}|/(0.5(1-r_{ol})L))^2)$, so the resulting field is essentially continuously differentiable at the edges of each patch.

One final step is involved in preparing a high resolution grid suitable for making tidal predictions, which is masking off regions where the estimate is thought to be inaccurate. This is done using the formal error estimate of the M_2 harmonic constants determined from altimetry, averaged over 500 km. The mask is set to zero where the mean standard error is greater than $\sigma_m = 2.75$ mm, a value which was subjectively determined. Additional criteria that result in a grid cell being masked off are the following: (1) fewer than 1250 data points used in the determination, (2) water depth less than 500 m, based on the GEBCO bathymetry (Weatherall et al. 2015), (3) less than 12 km distance to land, and (4) poleward of 60° latitude. As a final step, the discrete-valued mask is convolved with a compactly supported, twice-continuously differentiable function (Wendland

1995) in order to smooth the mask over 3°. In general the mask delimits regions where the mapped field appears to be spurious; however, it would be advantageous to optimize the mask using more objective criteria in the future.

4. Assessment of Baroclinic Tide Estimates

Figure 5 shows the M_2, S_2, K_1, and O_1 tides obtained with the approach described above, plotting the elevation in-phase with the Greenwich phase of the astronomical tidal potential (Simon 2013). The estimates obtained for the M_2, S_2, K_1, and O_1 baroclinic tides are superficially similar to those shown in previous works (Dushaw 2015; Zhao et al. 2016; Ray and Zaron 2016; Zhao 2017) but they differ in quantitative detail. The most conspicuous difference is the better representation of the M_2 tide in the Western Pacific, where the spatial aliasing of the tidal wavelength on the satellite ground tracks caused it to be reduced in previous efforts which utilized along-track spatial smoothing. In addition, the signal model of the present approach appears to admit more small-scale detail than previous estimates; although, a dedicated intercomparison effort is still ongoing (Loren Carrère, personal communication; Carrère et al. 2018). The detail visible in the S_2 field (Fig. 5b) is considerably reduced compared to that of M_2. This occurs because the map uses less data for S_2 compared with M_2, but also the amplitude of S_2 is lower and closer to the noise level. The way the spatial model is constructed essentially has a small-signal cutoff to avoid over-fitting the data.

Maps of the annual modulates of M_2 in Figure 6 are a new component of this work. The baroclinic MA_2 and MB_2 tides are generally too small to estimate reliably, so a larger fitting window has been used, and the result is heavily weighted towards their values from missions in the TOPEX/Poseidon reference orbit. The Arabian Sea, the region between the Seychelles and Madagascar, and the region offshore of the Amazon River Plume are locations where seasonal modulations are detectable (Fig. 6a). Seasonal modulation of the internal tides in the South China Sea have been studied previously, and attributed to the seasonal cycle of upper ocean stratification (Fig. 6b; Jan et al. 2008). The present maps essentially provide a regional view of these changes, which are present throughout the Western Pacific. Note that baroclinic and barotropic tidal seasonality has been identified previously using altimeter data (Müller et al. 2014).

A comparison of the present estimates of M_2 with a similar estimate published in Ray and Zaron (2016), also at $1/20°$-resolution, is shown in Figure 7. Denote the present estimate as HRET, for "High Resolution Empirical Tide", and the Ray and Zaron (2016) estimate as IT, for "Internal Tide." The difference of the in-phase components, HRET minus IT, is smaller than a few millimeters over much of the ocean, but differences exceeding a centimeter occur in the Western Pacific and in a few other regions where amplitudes are large and wavenumbers are zonal. The differences display a distinct pattern of satellite ground tracks and indicate that the estimates are in best agreement along the tracks (not shown); however, in regions where the wavenumber is zonal, the difference is not a random error, but it consists of propagating waves. This difference for zonal waves is thought to be caused by the along-track filtering used by Ray and Zaron (2016) to reduce the influence of long-wavelength errors, but it also tends to filter the waves oriented perpendicular to the satellite ground tracks. The present approach is based on fitting a model of sea-surface slope, so no explicit along-track filtering is necessary.

Figure 8 illustrates the usefulness of the separate tide models for de-aliasing tides in independent altimeter data. The variance reduction of the CryoSat-2 altimeter SSH measurements is plotted using data from 2012–2018, averaging within 2° lat.–lon. bins (more than 10,000 measurements per bin). Positive values (red) indicate the degree to which the predicted tides remove aliased tidal variability, while negative values (blue) indicate that noise is added by the tide model. The maximum variance explained within any bin is 13 cm^2 for M_2, but the mean variance is only

0.25 cm^2. There are a few locations, particularly to the south of the Kuroshio, where the explained variance is negative, but this is a region where fewer CryoSat-2 data are available due to changes in its data collection mask, so the significance of these variance estimates is reduced. S_2 explains a much smaller amount of variance, essentially all within the $\pm 30°$ latitude range displayed. The model for K_1 explains a maximum of 4 cm^2 variance, almost all in the seas of the Western Pacific.

The model is less successful in explaining variance at the O_1, MA_2, and MB_2 frequencies (Fig. 8d-f). These are smaller tides, but there are more regions where the tidal correction fails to reduce the variance. Nonetheless, the fields indicate a few regions where these tides are large enough that they might be considered for use as tidal corrections, depending on the specific application. The variance reduction from the total of the tidal corrections is dominated by the M_2 and K_1 components (Fig. 8g).

5. Baroclinic Tidal Dynamics

The previous section focussed on the sea-surface height expression of baroclinic tides. Potentially more insight into the dynamics can be obtained by studying the baroclinic tidal currents. Let $\mathbf{u} = (u, v)$ represent the horizontal current vector at the ocean surface. The instantaneous tidal currents ought to be related to the surface elevation through the equations,

$$\mathbf{u}_t + f\hat{k} \times \mathbf{u} = -g\nabla\eta + \mathbf{T}(\mathbf{u}, \mathbf{u}_o), \tag{4}$$

where $\mathbf{T}(\mathbf{u}, \mathbf{u}_o)$ is a vector which is a nonlinear function of both tidal currents and non-tidal currents, with the latter denoted by $\mathbf{u}_o$. The relationship between the mean, phase-locked, tidal currents and the surface elevation is, in principle, more complicated because it involves the projection of the above dynamics onto particular tidal frequencies,

$$-i\omega_j \mathbf{u}_j + f\hat{k} \times \mathbf{u}_j = -g\nabla\eta_j + \widehat{\mathbf{T}}_j(\mathbf{u}, \mathbf{u}_o), \tag{5}$$

where it is understood that $\mathbf{u}_j$ and η_j now refer to complex-valued fields associated with the j-th tidal frequency, ω_j, and $\widehat{\mathbf{T}}_j$ is analogous to the divergence of a Reynolds stress.

The physical effects represented by $\widehat{T}$ can be thought of as tidal self-interactions, such as shear-driven mixing (St. Laurent and Nash 2004), scattering by topography (Johnston et al. 2003), or sub- and super-harmonic generation (MacKinnon and Winters 2005; Wunsch 2017); and tidal/mean-flow interactions, such as time-dependent refraction (Rainville and Pinkel 2006; Park and Watts 2006) or directional scattering by geostrophic modes (Ward and Dewar 2010). For the essentially low-mode description of the tidal elevation which can be inferred from altimetry, it is hypothesized that time-dependence of the propagation medium is the dominant physical process, and it can be approximated by the linear relationship,

$$\widehat{\mathbf{T}}_j(\mathbf{u}, \mathbf{u}_o) = -\lambda_j \mathbf{u}_j, \tag{6}$$

where λ_j^{-1} is a damping time scale. One can estimate λ_j from the effective diffusivity of the non-tidal flow, $\nu_o = c_o L_o$, where c_o and L_o are the root-mean-square phase speed perturbation and its decorrelation scale, respectively. Then, $\lambda_j = \nu_o k_j^2$, where k_j is the wavenumber of internal tide. Plausible estimates for c_o range from 0.05 m/s to 0.1 m/s (Zaron and Egbert 2014; Buijsman et al. 2016), with a correlation scale of 100 km to 400 km (Zaron and Egbert 2014). Assuming a mid-latitude value of $k_j = 4.2 \times 10^{-5}$ m^{-1} for a mode-1 baroclinic semi-diurnal tide, the value of λ_{M2} ranges from 8×10^{-6} s^{-1} to 6×10^{-5} s^{-1}, a range of 5% to 50% of the M_2 frequency. For K_1, one would expect λ_{K1} to be about a factor of 4 smaller because of the approximately double wavelength.

A test of the hypothesized dynamics, equations (5)–(6), has been conducted by predicting baroclinic tidal currents and comparing them with currents inferred from surface drifters. The data set consists of 96 million hourly current vectors from twelve thousand drogued drifters, collected from 1995 to 2015 as a part of the NOAA Global Drifter Program (Elipot et al. 2016). Observed currents are compared with predicted tidal currents, and the variance reduction is used as a measure of the goodness-of-fit. Figure 9 shows the explained variance as a map, averaged within 2.5° bins, when no damping is assumed ($\lambda_j = 0$). For the largest and most accurately determined tides, M_2 and K_1, the model explains a positive amount of vector current variance almost everywhere.

Several points of interest can be noted from Figure 9. Comparison of the observed root-mean-square surface speed (Fig. 9a) with either of the root-mean-square predicted speeds (Fig. 9b and d), indicates that the predicted tidal currents are generally a small fraction of the observed currents; although, in a few areas, such as in Luzon Strait, near the Seychelles, near New Zealand, and off the North American west coast, the tidal currents may comprise 20% or more of the total. Also, since the tidal currents are related to the gradient of sea surface height, the M_2 currents look quite different from the M_2 surface elevation (Fig. 9b versus Fig. 5a). Close inspection of the explained current variance does highlight a few sites where the tide model has problems. The M_2 model adds variance (negative explained variance) at a few spots in the North Pacific and at several other locations near the coast (Fig. 9c, regions colored blue). The Gulf of Mexico is a region where the K_1 predictions are not accurate (Fig. 9e).

The GDP data set is large enough that it can discriminate between small adjustments to the dynamics. For example, the latitude-dependent acceleration of gravity, g, which varies by about 0.5% from pole to equator, is used in equation (5) (Moritz 2000). If a constant nominal value is used instead, $g = 9.81$ m^2/s, the area averaged explained variance is reduced slightly.

Figure 10 shows the explained variance as a function of λ_j for the M_2 and K_1 tides. The predictions for the other tides are not accurate enough to usefully constrain the damping time scale. The explained variance is maximized for $\lambda_{M2} = 2 \times 10^{-5}$ and $\lambda_{K1} = 10^{-5}$ (Fig. 10a), values which are within the range proposed above. As is evident from Figure 9, the geographic distribution of M_2 and K_1 currents is very different, so these variance-maximizing values of λ_j are measuring different physical locations. If, instead, the explained variance is restricted to the latitude range that includes Luzon Strait, where both M_2 and K_1 are relatively large, the optimal values are $\lambda_{M2} = 2 \times 10^{-5}$ and $\lambda_{K1} = 0.5 \times 10^{-5}$ (Fig. 10b), approximately $\lambda_{M2} = 4\lambda_{K1}$, as predicted. The ratio of these coefficients varies somewhat when averaging over different regions when other conditional averages are used; however, the general property of $\lambda_{M2} > \lambda_{K1}$ has been observed in every case examined.

6. Discussion

The maps of the low-mode M_2, S_2, and K_1 baroclinic tides presented here appear to be an incremental refinement of other published estimates (Zhao et al. 2016; Ray and Zaron 2016; Zhao 2017). Compared to these previously-published models, the HRET model involves small changes in the signal model, fitting the model to sea-surface slope rather than height, a slight increase in the quantity of data, and improved estimation and removal of non-tidal variability prior to harmonic analysis. The mapping methodology was inspired by the plane-wave fitting approach implemented by Zhao et al. (2016), which it sought to generalize and improve.

It is interesting to compare the present approach with one which uses the dynamics directly (e.g., Zaron et al. 2009). For the M_2 tide, the present approach estimates a maximum of 144 parameters per $(250\text{km})^2$ analysis window (6 wavenumbers $\times$ 2 modulus and direction $\times$ 6 spatial polynomial coefficients $\times$ 2 in-phase and quadrature parts). Typically, this involves about 3600 harmonic constants, or about 25 data points per parameter to be estimated. If only 3 wavenumbers were identified in the model-building stage, then there would be 50 data per parameter. This differs from the dynamics-based approach where the number of parameters to be estimated is determined by the model's spatial resolution and the assumed decorrelation scale of model errors. If the in-phase and quadrature components of the errors in the horizontal momentum equations were to be estimated, and a correlation scale of 50 km were assumed, there would be at least 200 parameters to estimate. This is roughly twice as many parameters as with the present approach, and easily 3 to 6 times as many in regions with relatively few waves. Thus, the highly structured signal model using relatively few degrees of freedom, with the vector wavenumber set by the preliminary model building (a nonlinear estimator), seems to be an advantage compared to more general dynamics-based approaches (Carrère et al. 2018).

Nonetheless, it is clear that the present approach has limitations which will cause it to lose utility near abrupt topography or where the baroclinic wave field deviates from the rudimentary signal model. Figure 11 illustrates the K_1 harmonic constants in a region of Western Pacific where the Philippine Sea meets the East China Sea. The boundary between the baroclinic waves (in the deep water) and their absence (on the continental shelf) is apparent. Capturing this spatial structure with the signal model of equation (1) is not possible, at least within analysis windows containing a sufficient quantity of data. Instead, it seems likely that subsequent improvements will result from using a more dynamically-constrained approach, but with a highly-structured error covariance model to reduce the number of parameters involved.

The damping time scale of 10^5 s (or 1.2 d) estimated in Section 5 agrees with the residence time of 1–1.5 days estimated by Zhao et al. (2016), based on their mode-1 M_2 tide map and the rate of energy input by the barotropic tide (Egbert and Ray 2001, 2003). Of course the present estimate is based on completely independent data and methodology, so it provides a check on the previous energy budget summaries (Wunsch and Ferrari 2004; Garrett and Kunze 2007).

The values of λ_j estimated above were obtained by maximizing a goodness-of-fit metric, which implicitly emphasizes those spatial regions with the largest baroclinic tidal kinetic energy. Thus, the area average damping time scale of the coherent tide could be greater or less than the inferred value, and it is difficult to place confidence limits on it, or map its spatial structure, without a detailed consideration of the physical mechanisms it represents. Such an analysis shall be the subject of future studies.

The form of the damping, $-\lambda_j \mathbf{u}_j$, was justified as a model for the loss of energy from the phase-locked tide, but it may alternately be regarded as an energy source for the non-phase-locked tide. The non-phase-locked tide obeys an energy equation, which could be written as

$$\nabla \cdot (\mathbf{c}_g^{(j)} E'_j) = \lambda_j \overline{E}_j - \gamma E'_j, \tag{7}$$

where $\mathbf{c}_g^{(j)}$ is the group velocity and E'_j and $\overline{E}_j$ are the non-phase-locked and phase-locked wave energy, respectively, associated with the j-th tidal frequency. This expression can be integrated over the deep ocean, bounded by the continental margins, to obtain,

$$(1 - r_j) P \mathbf{c}_g^{(j)} E'_j = \lambda_j A \overline{E}_j - \gamma_j A E'_j, \tag{8}$$

where r_j is the reflection coefficient for the low-mode baroclinic tide at the continental margin, about 0.4 (Kelly et al. 2013), P is the perimeter of the deep ocean, and A is the surface area of the ocean. At this level of approximation the quantities E_j and $\overline{E}_j$ are regarded as area averages, and γ_j^{-1} is a damping time for the non-phase-locked time.

The global mean ratio of non-phase-locked to phase-locked baroclinic tidal variance, $E'_{M2}/\overline{E}_{M2}$, is estimated as 0.5 (Zaron 2015, 2017). Equation (8) can be re-arranged to compute this same quantity,

$$\frac{E'_j}{\overline{E}_j} = \left((1 - r_j) \frac{P}{A} \frac{\mathbf{c}_g^{(j)}}{\lambda_j} + \frac{\gamma_j}{\lambda_j} \right)^{-1}. \tag{9}$$

One expects the ratio, P/A, to be some multiple of the reciprocal of R_e, the radius of the earth, and $\mathbf{c}_g^{(j)}/\lambda_j$ is a measure of the propagation distance of the phase-locked tide, only about $0.05 R_e$ using a mean group speed of $c_g^{(M2)} = 2.5$ m/s and $\lambda_{M2} = 10^{-5}$ s^{-1}. Even with a generous estimate for the perimeter, P, across which the tides are reflected or dissipate, the ratio P/A does not seem much larger than about $4/R_e$, so the first term in the above expression is apparently smaller than 1/8. If the ratio $E'_j/\overline{E}_j$ is to be smaller than 1, then the non-phase-locked tide must be rapidly damped, with γ_j the same size or larger than λ_j.

It is hard to reconcile the estimate $\gamma_j = \lambda_j$ with known mechanisms of dissipation for the low-mode tide. It is possible that estimates of $E'_{M2}/\overline{E}_{M2}$ from altimetry are biased low (Zaron 2015, 2017). They are obtained from analysis of variance, which means they are implicitly weighted towards areas with the largest signals, presumably the generation sites where the non-phase-locked tide would be smaller than average. Estimates from moorings are not inconsistent with a larger value, $E'_j/\overline{E}_j = 4$ (Alford and Zhao 2007), but even this is not large enough to constrain $\gamma_j \ll \lambda_j$. Perhaps the $E'_j \gg \overline{E}_j$ regime described by Weisberg et al. (1987) is more typical.

Alternately, it is possible that the same factors causing the loss of coherence of the internal tide also result in the formation of caustics where the higher amplitudes and nonlinearity could lead to a rapid transfer of energy into the broadband internal wave spectrum (Zhao and D'Asaro 2011; Dunphy and Lamb 2014). Laboratory studies with coherent internal wave sources find that the rapid transfer of energy out of the phase-locked waves is enabled by lateral inhomogeneity in the wave field (Bordes et al. 2012).

7. Summary

A new series of models for the phase-locked component of the low-mode-baroclinic M_2, S_2, K_1, and O_1 tides, and the annual modulations of the M_2 tide, have been developed. The models differ from previous efforts in minor respects. While development and intercomparison is an ongoing exercise, it appears that the present results are slightly more accurate than other published and un-published models (Carrère et al. 2018). For example, the root-mean-square variance reduction of the present M_2 solution exceeds that of Ray and Zaron (2016) by only about 2 mm globally; however, larger differences exceeding 2.5 cm are present at specific sites (Loren Carrère, personal communication). Further improvements in satellite altimetry and processing techniques, and innovations in mapping techniques, will certainly lead to further increases in accuracy in the future.

The primary purpose of this manuscript is to document the mapping technique and validate the tide models using a large surface current drifter dataset. The latter leads to a new estimate for the scattering rate of the phase-locked tide, with implications for the generation and dissipation of the non-phase-locked tide.

The present model should be useful for removing aliased tidal signals from satellite altimeter measurements and in situ measurements of various kinds (Zaron and Ray 2017). The former should facilitate more accurate mapping of mesoscale sea level anomalies (Fu et al. 2010), including the identification of barotropic tidal energetics within small regions (Zaron and Egbert 2006). Tandem studies of barotropic and baroclinic tidal energetics, based on the present models, can be expected to lead to more rigorous bounds on the energetics than presented in Section 6 and should be considered in the future.

Acknowledgments. The along-track altimetry data were obtained using the Radar Altimeter Database System (RADS), `http://rads.tudelft.nl/rads/rads.shtml`, which is an effort of the Department of Earth Observation and Space Systems at TU Delft and the NOAA Laboratory for Satellite Altimetry. The surface drifter data were collected and distributed via the NOAA Global Drifter Program (`http://www.aoml.noaa.gov/phod/dac/gdp_information.php`). Computations were performed using the Portland Institute for Computational Science cluster computer, *Coeus*, acquired with support from NSF award #DMS1624776 and ARO award

#W911NF-16-1-0307. Further support was provided by the National Geospatial-Intelligence Agency award #HM0177-13-1-0008 and NASA awards #NNX16AH88G and #NNX17AJ35G.

References

Alford, M. H., R.-C. Lien, H. Simmons, J. Klymak, S. Ramp, Y. J. Yang, D. Tang, and M.-H. Chang, 2010: Speed and evolution of nonlinear internal waves transiting the South China Sea. *J. Phys. Oceanogr.*, **40**, 1338–1355.

Alford, M. H., and Z. Zhao, 2007: Global patterns of low-mode internal-wave propagation. Part I: energy and energy flux. *J. Phys. Oceanogr.*, **37**, 1829–1848.

Andersen, O. B., 1995: Global ocean tides from ERS-1 and T/P altimetry. *J. Geophys. Res.*, **100 (C12)**, 25 249–25 259.

Anonymous, 2014: A new verson of SSALTO/DUACS products available in April 2014, version 1.1, accessed 2018-09-04 from https://www.aviso.altimetry.fr/fileadmin/documents/data/duacs/Duacs2014.pdf.

Baines, P. G., 1982: On internal tide generation models. *Deep Sea Res.*, **29**, 307–338.

Bordes, G., A. Venaille, S. Joubaud, P. Odier, and T. Dauxois, 2012: Experimental observation of a strong mean flow induced by internal gravity waves. *Phys. Fluids*, **24**, 086 602.

Bozdogan, H., 1987: Model selection and Akaike's Information Criterion (AIC): the general theory and its analytical extensions. *Psychometrika*, **52 (3)**, 345–370.

Buijsman, M. C., and Coauthors, 2016: Impact of parameterized internal wave drag on the semidiurnal energy balance in a global ocean circulation model. *J. Phys. Oceanogr.*, **46 (5)**, 1399–1419.

Carrère, L., C. Le Provost, and F. Lyard, 2004: On the statistical stability of the M_2 barotropic and baroclinic tidal characteristics from along-track TOPEX/Poseidon satellite altimetry analysis. *J. Geophys. Res.*, **109 (C3)**, c03033.

Carrère, L., and Coauthors, 2018: Review: A review of new internal-tides models and validation results, 25 Years of Progress in Radar Altimetry, Ponta Delgada, Azores.

Cherniawsky, J. Y., M. G. G. Foreman, W. R. Crawford, and R. F. Henry, 2001: Ocean tides from TOPEX/Poseidon sea level data. *J. Atm. and Ocean. Tech.*, **18**, 649–664.

Doodson, A. T., and H. D. Warburg, 1941: *Admiralty Manual of Tides*. Hydrography Department, Admiralty, Her Majesty's Stationary Office, London, 270 pp.

Dunphy, M., and K. G. Lamb, 2014: Focusing and vertical mode scattering of the first mode internal tide by mesoscale eddy interaction. *J. Geophys. Res.*, **119 (1)**, 523–536.

Dushaw, B., 2015: An empirical model for mode-1 internal tides derived from satellite altimetry: Computing accurate tidal predictions at arbitrary points over the world oceans. Tech. Rep. APL-UW TM 1-15, University of Washington Applied Physics Laboratory, 114 pp.

Egbert, G. D., and R. D. Ray, 2000: Significant tidal dissipation in the deep ocean inferred from satellite altimeter data. *Nature*, **405**, 775–778.

Egbert, G. D., and R. D. Ray, 2001: Estimates of M_2 tidal energy dissipation from TOPEX/POSEIDON altimeter data. *J. Geophys. Res.*, **106 (C10)**, 22,475–22,502.

Egbert, G. D., and R. D. Ray, 2003: Semi-diurnal and diurnal tidal dissipation from TOPEX/POSEIDON altimetry. *Geophys. Res. Lett.*, **30 (17)**, 1907–1910.

Egbert, G. D., R. D. Ray, and B. G. Bills, 2004: Numerical modeling of the global semidiurnal tide in the present day and in the last glacial maximum. *J. Geophys. Res.*, **109**, C03 003.

Elipot, S., R. Lumpkin, R. C. Perez, J. M. Lilly, J. J. Early, and A. M. Sykulski, 2016: A global surface drifter data set at hourly resolution. *J. Geophys. Res.*, **65 (1)**, 29–50.

Fu, L., D. Chelton, P.-Y. LeTraon, and R. Morrow, 2010: Eddy dynamics from satellite altimetry. *Oceanography*, **23 (4)**, 14–25.

Fu, L.-L., and A. Cazenave, Eds., 2001: *Satellite Altimetry and Earth Sciences*, International Geophysics Series, Vol. 69. Academic Press, San Francisco, 463 pp.

Garrett, C., and E. Kunze, 2007: Internal tide generation in the deep ocean. *Annu. Rev. Fluid Mech.*, **39**, 57–87.

Gaultier, L., C. Ubelmann, and L.-L. Fu, 2016: The challenge of using future SWOT data for oceanic field reconstruction. *J. Atm. and Ocean. Tech.*, **33 (1)**, 119–126.

Huess, V., and O. B. Andersen, 2001: Seasonal variation in the main tidal constituent from altimetry. *Geophys. Res. Lett.*, **28 (4)**, 567–570.

Jan, S., R. Lien, and C. Ting, 2008: Numerical study of baroclinic tides in Luzon Strait. *J. Oceanogr.*, **64**, 789–802.

Jenkins, G. M., and D. G. Watts, 1968: *Spectral Analysis and its Applications*. Holden Day, Oakland, California, 525 pp.

Johnston, S. T., M. A. Merrifield, and P. E. Holloway, 2003: Internal tide scattering at the Line Islands Ridge. *J. Geophys. Res.*, **108 (C11)**, 3365.

Kantha, L. H., and C. C. Tierney, 1997: Global baroclinic tides. *Prog. Oceanogr.*, **40**, 163–178.

Kelly, S. M., 2016: The vertical mode decomposition of tides in the presence of a free surface and arbitrary topography. *J. Phys. Oceanogr.*, **46**, 3777–3788.

Kelly, S. M., N. L. Jones, J. D. Nash, and A. F. Waterhouse, 2013: The geography of semidiurnal mode-1 internal-tide energy loss. *Geophys. Res. Lett.*, **40**, 4689–4693.

Legg, S., and K. M. Huijts, 2006: Preliminary simulations of internal waves and mixing generated by finite-amplitude tidal flow over isolated topography. *Deep Sea Res. II*, **53**, 140–156.

Lyszkowicz, A. B., and A. Bernatowicz, 2017: Current state of the art of satellite altimetry. *Geodesy and Cartography*, **66 (2)**, 259–270.

MacKinnon, J. A., and K. Winters, 2005: Subtropical catastrophe: significant loss of low-mode tidal energy at 28.9^o. *Geophys. Res. Lett.*, **32**, L15 605.

Melet, A., R. Hallberg, S. Legg, and K. Polzin, 2013: Sensitivity of the ocean state to the vertical distribution of internal-tide-driven mixing. *J. Phys. Oceanogr.*, **43**, 602–615.

Moritz, H., 2000: Geodetic Reference System 1980. The Geodesist's Handbook. *J. Geod.*, **74**, 128–133.

Müller, M., J. Cherniawsky, M. G. Foreman, and J.-S. von Storch, 2014: Seasonal variation of the M_2 tide. *Oc. Dyn.*, **64 (2)**, 159–177.

Park, J., and D. R. Watts, 2006: Internal tides in the Southwestern Japan/East Sea. *J. Phys. Oceanogr.*, **36**, 22–34.

Picot, N., S. Desai, J. Figa-Saldana, and R. Scharroo, 2014: Jason-2 Version 'D' Geophysical Data Records: Public Release, accessed 2014-12-01 from http://www.aviso.oceanobs.com/fileadmin/documents/data/tools/JA2_GDR_D_release_note.pdf.

Picot, N., S. Desai, J. Hausman, and E. Bronner, 2012: AVISO and PODAAC User Handbook IGDR and GDR Jason Products, accessed 2015-06-06 from http://www.aviso.altimetry.fr/fileadmin/documents/data/tools/hdbk_j1_gdr.pdf.

Pujol, M.-I., Y. Faugère, G. Taburet, S. Dupuy, C. Pelloquin, M. Ablain, and N. Picot, 2016: DUACS DT2014: the new multi-mission altimeter data reprocessed over 20 years. *Ocean Sci.*, **12**, 1067–1090.

Rainville, L., T. S. Johnston, G. S. Carter, M. A. Merrifield, R. Pinkel, P. F. Worcester, and B. D. Dushaw, 2010: Interference pattern and propagation of the M_2 internal tide south of the Hawaiian Ridge. *J. Phys. Oceanogr.*, **40**, 311–325.

Rainville, L., and R. Pinkel, 2006: Propagation of low-mode internal waves through the ocean. *J. Phys. Oceanogr.*, **36**, 1220–1236.

Ray, R. D., 1999: A global ocean tide model from Topex/Poseidon altimetry: GOT99.2. Tech. Rep. 209478, NASA Tech. Memo, Goddard Space Flight Center, Greenbelt, Maryland, 58 pp. URL https://ntrs.nasa.gov/search.jsp?R=19990089548.

Ray, R. D., and D. A. Byrne, 2010: Bottom pressure tides along a line in the southeast Atlantic Ocean and comparisons with satellite altimetry. *Ocean Dyn.*, **60**, 1167–1176.

Ray, R. D., and D. E. Cartwright, 2001: Estimates of internal tide energy fluxes from TOPEX/POSEIDON altimetry: Central North Pacific. *Geophys. Res. Lett.*, **28**, 1259–1262.

Ray, R. D., and G. T. Mitchum, 1996: Surface manifestation of internal tides generated near Hawaii. *Geophys. Res. Lett.*, **23**, 2101–2104.

Ray, R. D., and E. D. Zaron, 2011: Non-stationary internal tides observed with satellite altimetry. *Geophys. Res. Lett.*, **38**, L17 609, doi:10.1029/2011GL048617.

Ray, R. D., and E. D. Zaron, 2016: M_2 internal tides and their observed wavenumber spectra from satellite altimetry. *J. Phys. Oceanogr.*, **46**, 3–22.

Scharroo, R., E. W. Leuliette, J. L. Lillibridge, D. Byrne, M. C. Naeije, and G. T. Mitchum, 2013: RADS: Consistent multi-mission products. *Proc. of the Symposium on 20 Years of Progress in Radar Altimetry, Eur. Space Agency Spec. Publ., ESA SP-710,*, Venice, 20-28 September 2012, 4, URL http://rads.tudelft.nl/rads/rads.shtml.

Scott, R. B., and Y. Xu, 2009: An update on the wind power input to the surface geostrophic flow of the world ocean. *Deep Sea Res.*, **56 (3)**, 295–304.

Simon, B., 2013: *Coastal Tides*. Trans. by David Manley; Monaco: Institut Oceanographique, Paris, 409 pp.

St. Laurent, L. C., and J. D. Nash, 2004: An examination of the radiative and dissipative properties of deep ocean internal tides. *Deep Sea Res.*, **51**, 3029–3042.

Stammer, D., and Coauthors, 2014: Accuracy assessment of global barotropic ocean tide models. *Rev. of Geophys.*, **52 (3)**, 243–282.

Ward, M. L., and W. K. Dewar, 2010: Scattering of gravity waves by potential vorticity in a shallow-water fluid. *J. Fluid Mech.*, **663**, 478–506.

Weatherall, P., and Coauthors, 2015: A new digital bathymetric model of the world's oceans. *Earth and Space Science*, **2 (8)**, 331–345.

Weisberg, R. H., D. Halpern, T. Y. Tang, and S. M. Hwang, 1987: M_2 tidal currents in the Eastern Equatorial Pacific Ocean. *J. Geophys. Res.*, **92 (C4)**, 3821–3826.

Wendland, H., 1995: Piecewise polynomial, positive definite and compactly supported radial functions of minimal degree. *Adv. Comput. Math.*, **4**, 389–396.

Willis, J. K., L. L. Fu, E. Lindstrom, and M. Srinivasan, 2010: 17 years and counting: Satellite altimetry from research to operations. *2010 IEEE International Geoscience and Remote Sensing Symposium*, Honolulu, HI, 777–780.

Wunsch, C., and R. Ferrari, 2004: Vertical mixing, energy, and the general circulation of the oceans. *Ann. Rev. Fluid Mech.*, **36**, 281–314.

Wunsch, S., 2017: Harmonic generation by nonlinear self-interaction of a single internal wave mode. *J. Fluid Mech.*, **828**, 630–647.

Zaron, E. D., 2015: Non-stationary internal tides inferred from dual-satellite altimetry. *J. Phys. Oceanogr.*, **45 (9)**, 2239–2246.

Zaron, E. D., 2017: Mapping the non-stationary internal tide with satellite altimetry. *J. Geophys. Res.*, **122 (1)**, 539–554.

Zaron, E. D., C. Chavanne, G. D. Egbert, and P. Flament, 2009: Baroclinic tidal generation in the Kauai Channel inferred from HF-Radar. *Dyn. Atm. and Oceans*, **48**, 93–120.

Zaron, E. D., and G. D. Egbert, 2006: Estimating open-ocean barotropic tidal dissipation: the Hawaiian Ridge. *J. Phys. Oceanogr.*, **36**, 1019–1035.

Zaron, E. D., and G. D. Egbert, 2014: Time-variable refraction of the internal tide at the Hawaiian Ridge. *J. Phys. Oceanogr.*, **44 (2)**, 538–557.

Zaron, E. D., and R. D. Ray, 2017: Using an altimeter-derived internal tide model to remove tides from in-situ data. *Geophys. Res. Lett.*, **44**, 1–5.

Zaron, E. D., and R. D. Ray, 2018: Aliased tidal variability in mesoscale sea level anomaly maps. *J. Atm. and Ocean. Tech.*, *submitted*.

Zhao, Z., 2016: Using CryoSat-2 altimeter data to evaluate M_2 internal tides observed from multisatellite altimetry. *J. Geophys. Res.*, **121 (7)**, 5164–5180.

Zhao, Z., 2017: The global mode-1 S_2 internal tide. *J. Geophys. Res.*, **122 (11)**, 8794–8812.

Zhao, Z., M. H. Alford, and J. B. Girton, 2012: Mapping low-mode internal tides from multisatellite altimetry. *Oceanography*, **25 (2)**, 42–51.

Zhao, Z., M. H. Alford, J. B. Girton, L. Rainville, and H. L. Simmons, 2016: Global observations of open-ocean mode-1 M_2 internal tides. *J. Phys. Oceanogr.*, **46**, 1657–1684.

Zhao, Z., and E. A. D'Asaro, 2011: A perfect focus of the internal tide from the Mariana Arc. *Geophys. Res. Lett.*, **38**, L14 609.

LIST OF TABLES

TABLE 1. Satellite altimeter missions used. Abbreviations for the mission names follows usage in the Radar Altimeter Database System (Scharroo et al. 2013).

Satellite mission	Time period	Orbit cycles
(TOPEX/Jason reference orbit, $\Delta t = 9.9156$d)		
TXA	1992–2002	4–364
J1A	2002–2009	1–259
J2A	2008–2015	1–303
J3A	2016–2017	1–45
(TOPEX/Jason interleaved orbit, $\Delta t = 9.9156$d)		
TXB	2002–2005	369–480
J1B	2009–2012	262–374
J2B	2016–2017	305–327
(Geosat orbit, $\Delta t = 17.0505$d)		
G1A	2000–2008	37–223
(ERS/Envisat reference orbit, $\Delta t = 35.0000$d)		
E2A	1995–2011	1–164
N1B	2002–2010	10–94
SAA	2013–2017	1–34

TABLE 2. Alias periods [days] appear on the main diagonal. Synodic periods [days] are above the main diagonal. Synodic periods denoted 6793* indicate aliases which are separable over an 18.6 yr. nodal cycle, assuming the nodal modulation of MA_2 is the same as that of M_2.

	MA_2	M_2	MB_2	S_2	O_1	K_1
(TOPEX/Jason reference orbit, $\Delta t = 9.9156$d)						
MA_2	75	365	183	274	118	132
M_2		62	365	1104	173	97
MB_2			53	546	330	76
S_2				59	206	89
O_1					46	62
K_1						173
(Geosat orbit, $\Delta t = 17.0505$d)						
MA_2	170	365	183	6793*	337	5611
M_2		318	365	359	175	391
MB_2			2459	181	118	189
S_2				169	343	4378
O_1					113	318
K_1						175
(ERS/Envisat reference orbit, $\Delta t = 35.0000$d)						
MA_2	75	365	183	75	6793*	94
M_2		94	365	94	365	127
MB_2			127	127	183	196
S_2				∞	75	365
O_1					75	94
K_1						365

TABLE 3. Tide model parameters. Other parameters: maximum number of wavenumbers used, $N = 6$; order of polynomial, $P = 2$; tangent plane resolution, $\Delta x = 6$ km; fractional overlap of tangent planes, $1 - r_{ol} = 3/4$; 2-dimensional spectral window function and data weight, $\exp(-(5|\mathbf{x}|/L)^2))$; 2-dimensional spectra over-sampling factor, $f_{2D} = 3$; global lat.-lon. grid resolution, $\Delta\Theta = (1/20)^\circ$; 2-dimensional interpolation weight for gridding, $\exp(-(|\mathbf{x}|/(0.5(1 - r_{ol})L))^2)$

Darwin Symbol	Doodson number	Alias periods TX/G1/E2 [day]	Fitting window L [km]	Wavelength range L_{lo}–L_{hi} [km]
M_2	2 555 555	62/318/94	500	40–200
S_2	2 735 555	59/169/∞	1000	40–200
K_1	1 655 556	173/175/365	1000	90–450
O_1	1 455 554	46/113/75	1000	90–450
MA_2	2 545 555	75/170/75	1000	40–200
MB_2	2 565 555	53/2459/127	1000	40–200

LIST OF FIGURES

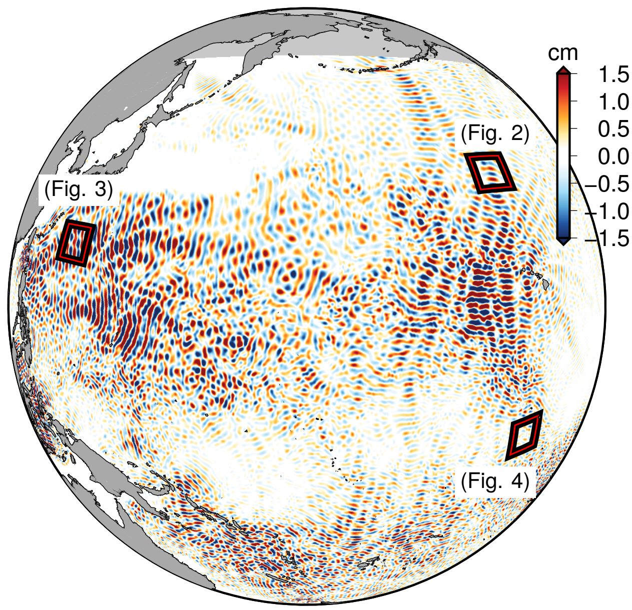

FIG. 1. Western Pacific basin — context for Figures 2-4. The in-phase component of the baroclinic M_2 tide is shown, estimated from altimetry using the methods described in the text. Rectangles indicate the regions used in Figures 2-4.

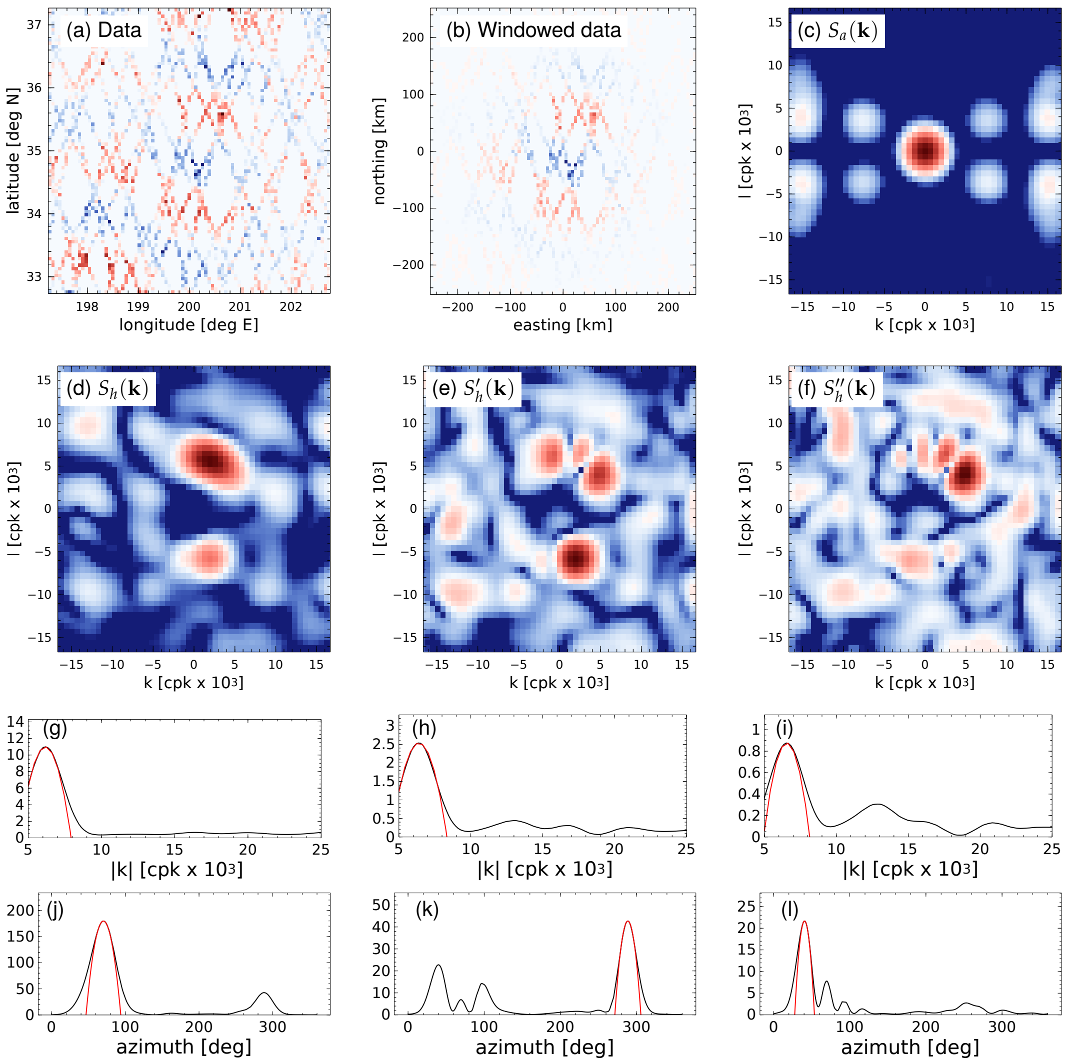

FIG. 2. Model building: determination of k_i and ϕ_i in a domain northeast of Hawaii. (a) Color scale shows the quadrature component (relative to Greenwich phase) of the M_2 harmonic constants along multiple satellite ground tracks ($\pm$1.5cm range). (b) Prior to spectral analysis, the data are spatially windowed, as shown. (c) The 2-dimensional power spectrum of the windowed sampling function shows how leakage occurs in the spectral domain. (d)-(f) The 2-dimensional power spectrum of the $h(\mathbf{x})$ function used in the first three plane wave fits (log-scaled, displaying 3 orders of magnitude). (g)-(i) One-dimensional radial wavenumber spectrum, the azimuthal integral of (d)-(f); units of $\mathrm{mm}^2/\mathrm{cpk}$. The de-noised spectrum (black) is used to determine the peak wavenumber, k_i, at the apex of the local quadratic fit (red). (j)-(l) Spectrum (black) integrated over the strip $[0.75, 1.25]k_i$ as a function of azimuthal angle, ϕ_i (local quadratic fit in red); units of $\mathrm{mm}^2/\mathrm{rad}$.

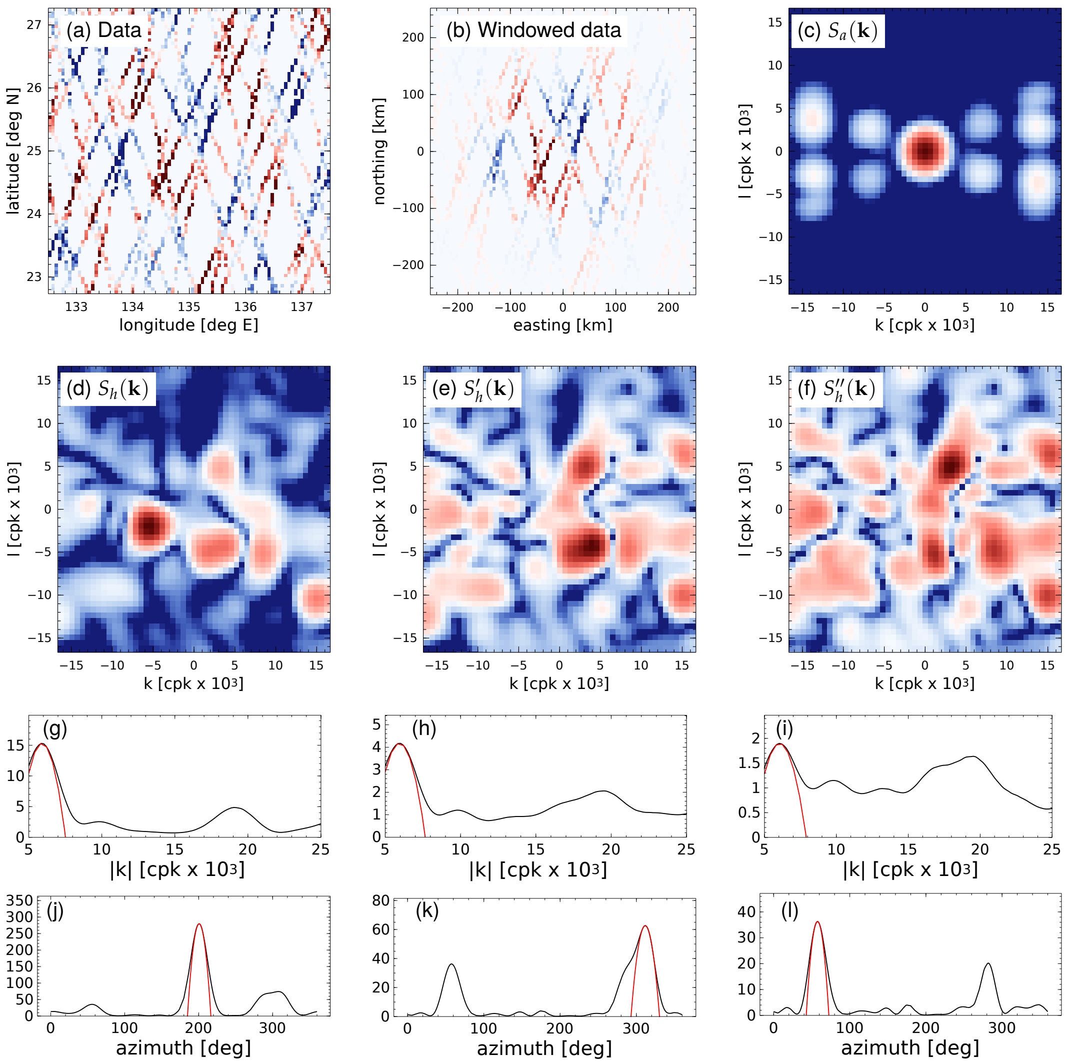

FIG. 3. Model building: determination of k_i and ϕ_i in the Subtropical Western Pacific. Panels as in Figure 2

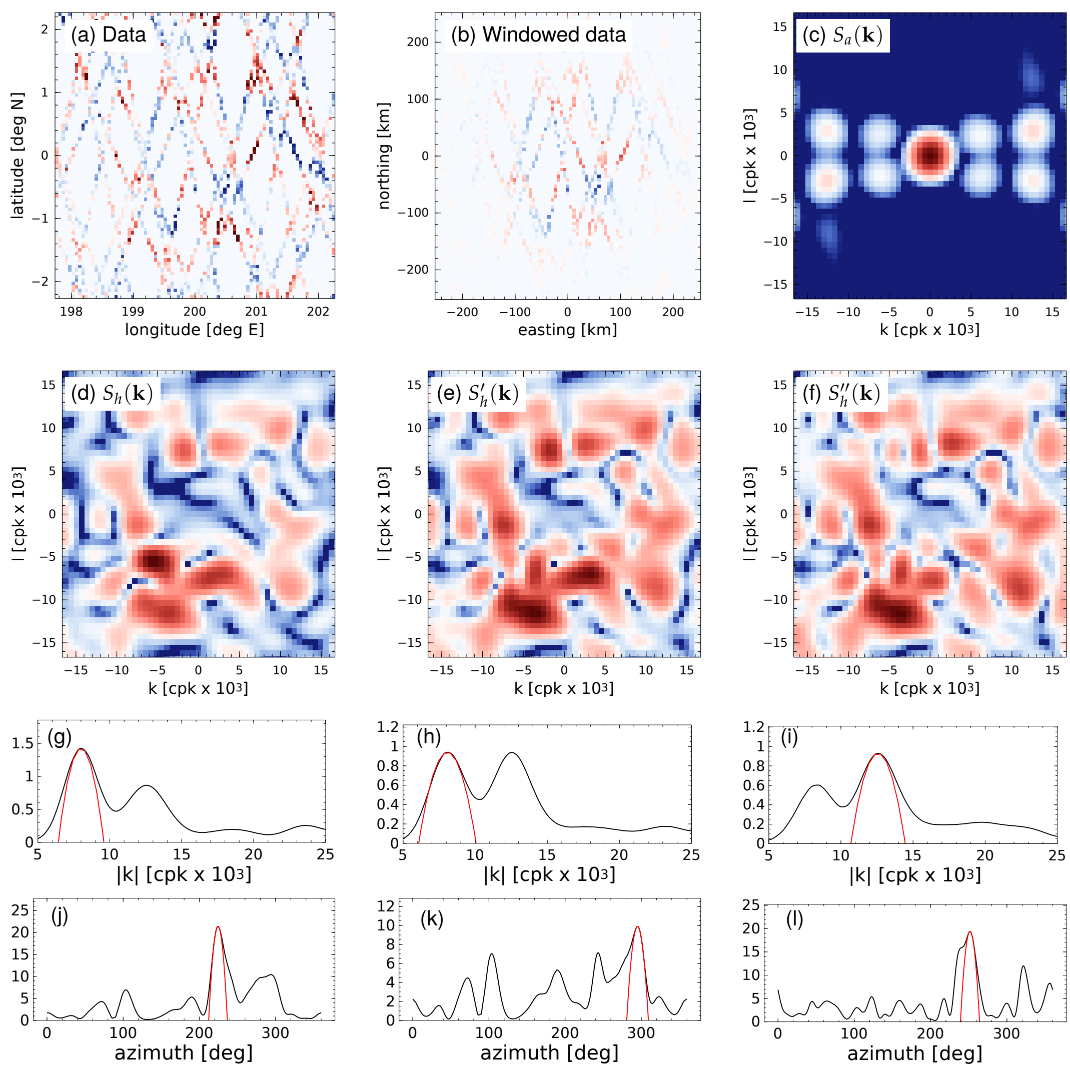

FIG. 4. Model building: determination of k_i and ϕ_i in the Equatorial Pacific. Panels as in Figure 2.

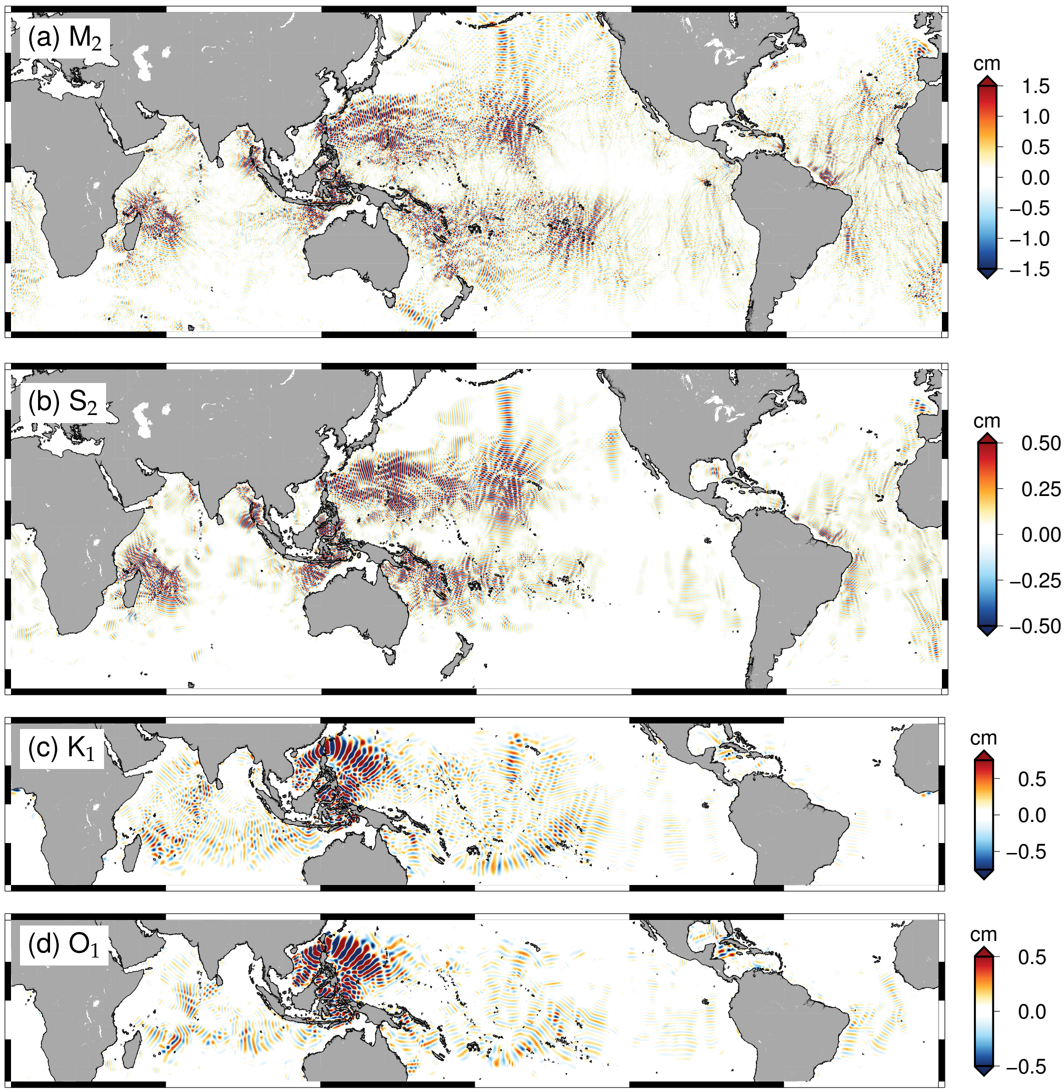

FIG. 5. Baroclinic tide estimates at $(1/20)^{\circ}$-resolution. The in-phase component of the four main tidal components is shown. Note the different color scales used in each panel. Latitude range shown is -50° to 55° in panels (a)-(b) and $\pm 30^{\circ}$ in panels (c)-(d). Unless otherwise labelled, 60° increments of longitude and 15° increments of latitude are indicated on the edges of the plots. Please refer to Supplementary Materials for detailed versions of these figure panels.

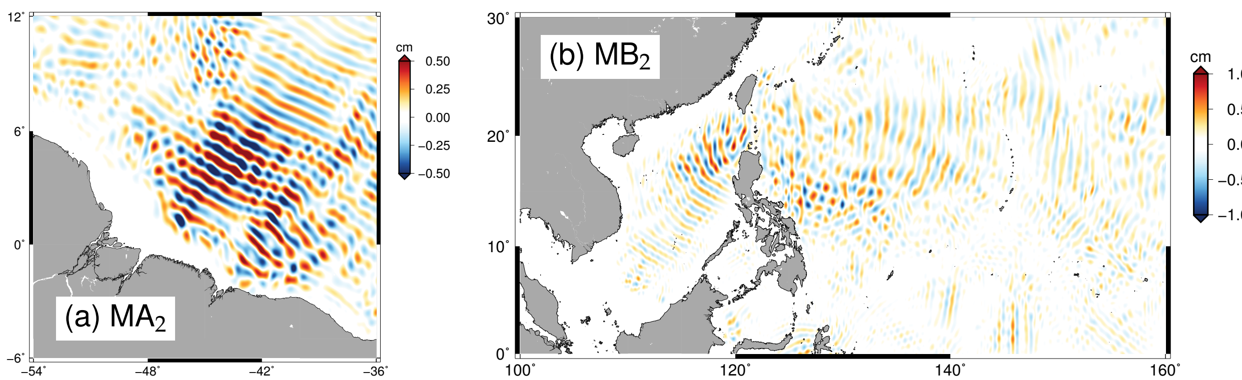

FIG. 6. In-phase components of the seasonal modulates of M_2 in regions where it is a substantial fraction of the size of M_2: (a) MA_2 offshore of the Amazon River plume, and (b) MB_2 in the South China Sea and Western Pacific.

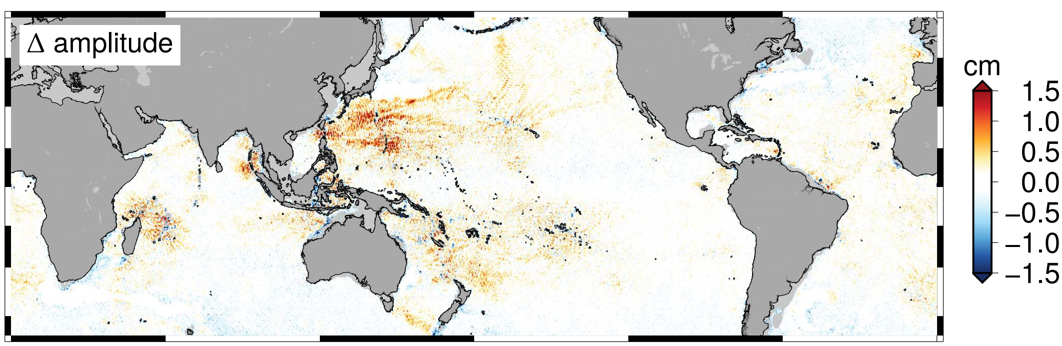

FIG. 7. Baroclinic M_2 tide amplitude comparison, the present work minus the estimate of Ray and Zaron (2016).

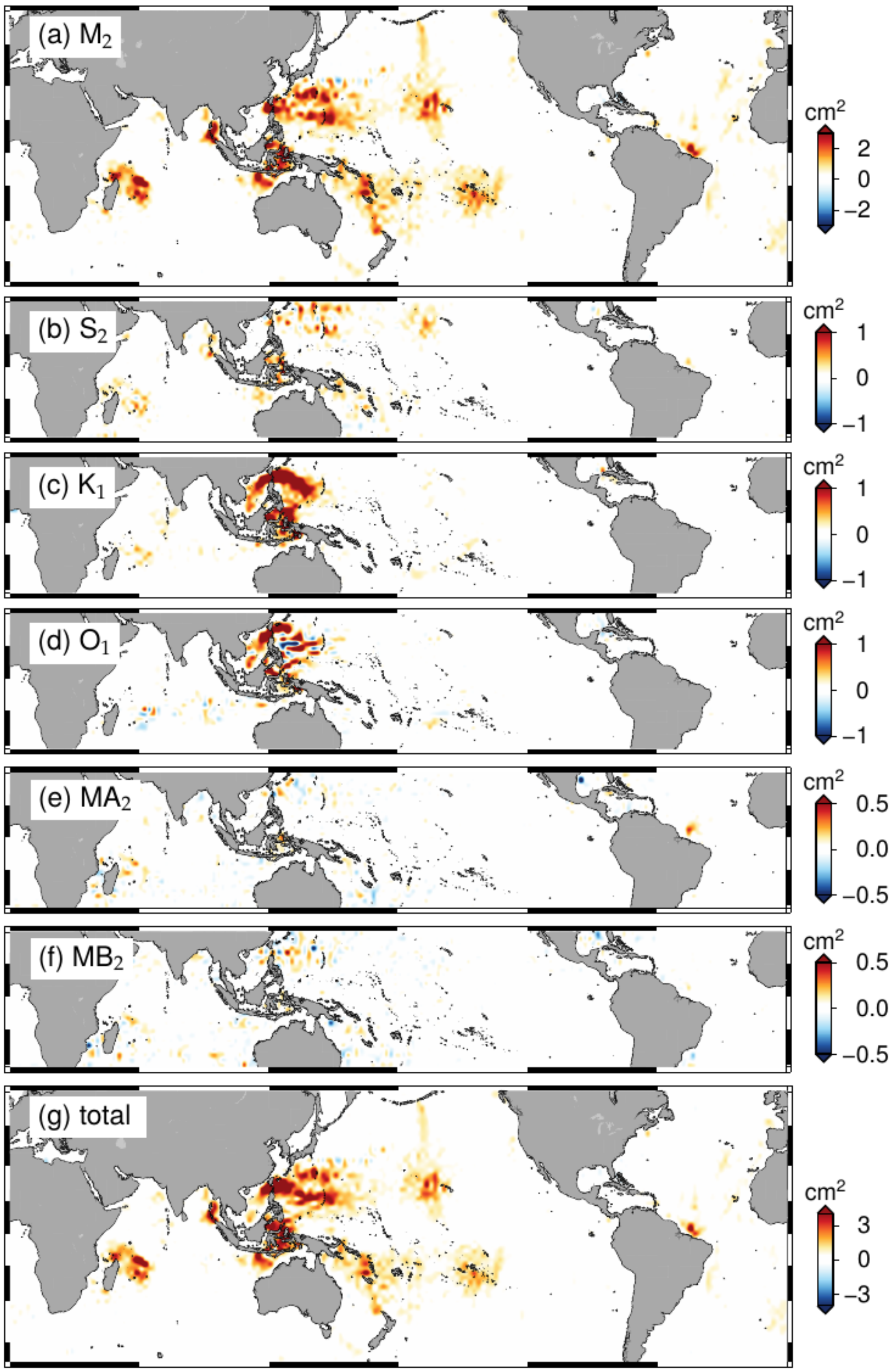

FIG. 8. Explained variance with respect to CryoSat-2. Red color indicates where the model successfully reduces variance and may be used as a correction to remove baroclinic tidal sea level variability. Latitude range shown is $-50°$ to $55°$ in panels (a) and (g); the range is $\pm30°$ in the other panels.

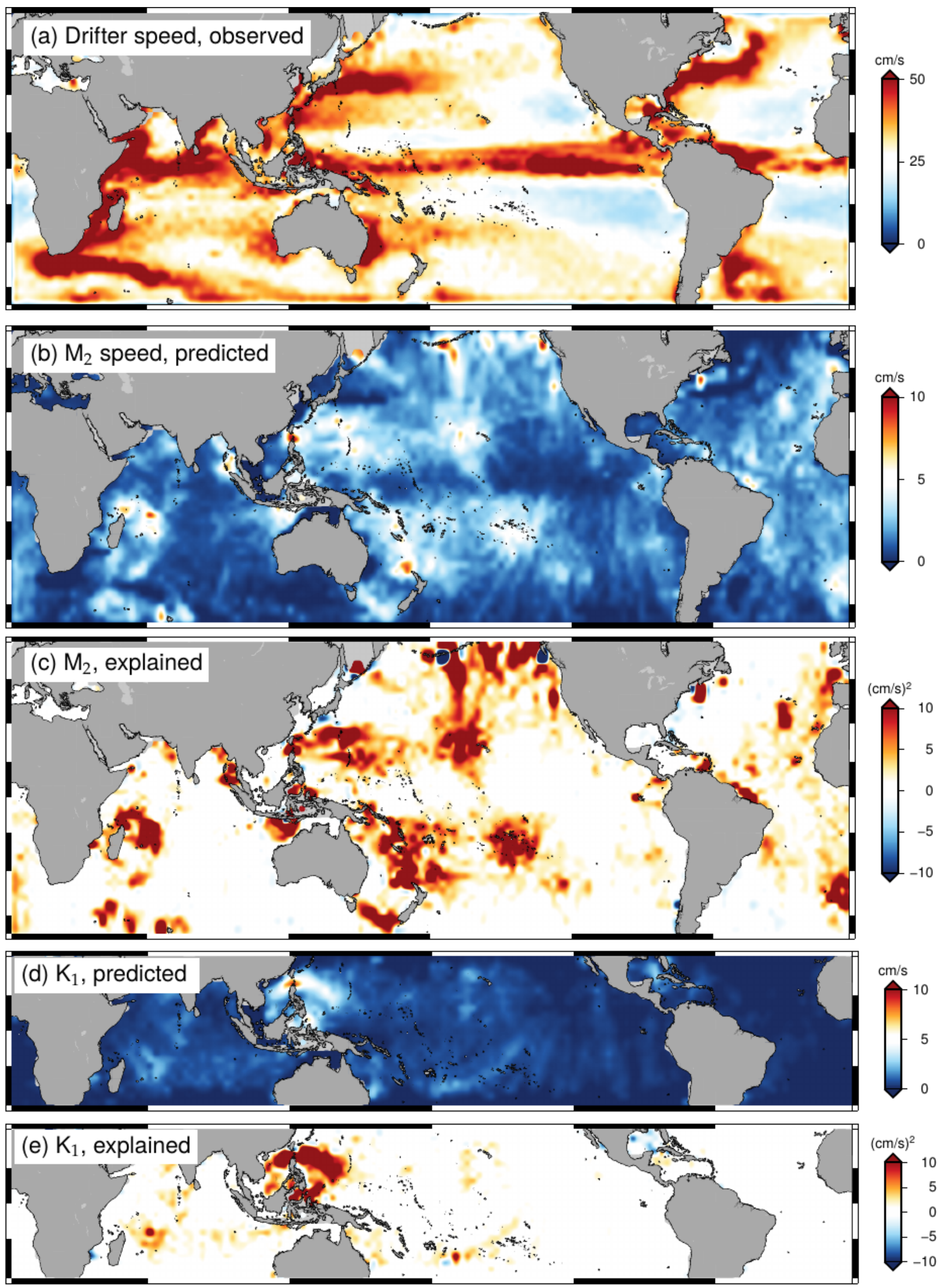

FIG. 9. Surface currents. Latitude range shown is $-50°$ to $55°$ in (a)–(c); the range is $\pm 30°$ in (d)–(e).

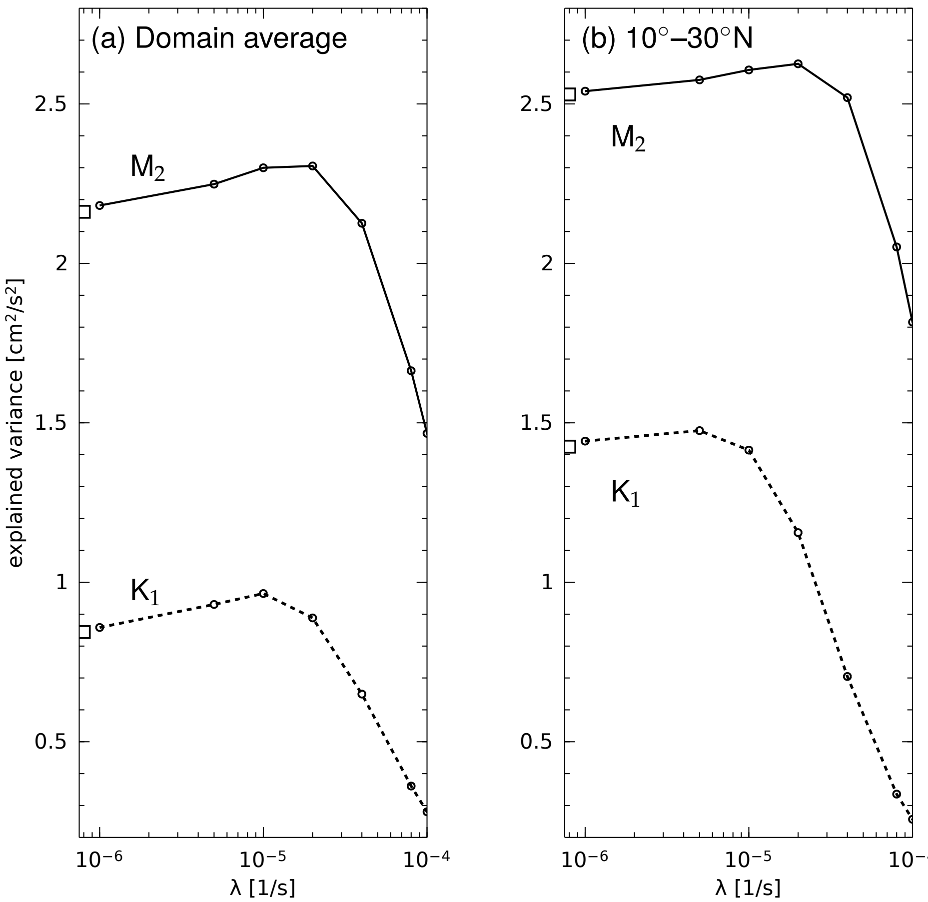

FIG. 10. Explained variance versus damping coefficient, λ_j. (a) Average of the explained variance over the latitude range, $-50°$ to 55°N, for M_2 and the range, $-30°$ to 30°N, for K_1. (b) Average of the explained variance over the latitude range, 10° to 30°N, for both M_2 and K_1. Theory predicts maximum explained variance will occur when $\lambda_{M2} = 4\lambda_{K1}$, approximately as observed when the explained variance is averaged over the same region for the two tides. The square symbol plotted next to the *y*-axis denotes the explained variance when $\lambda_j = 0$.

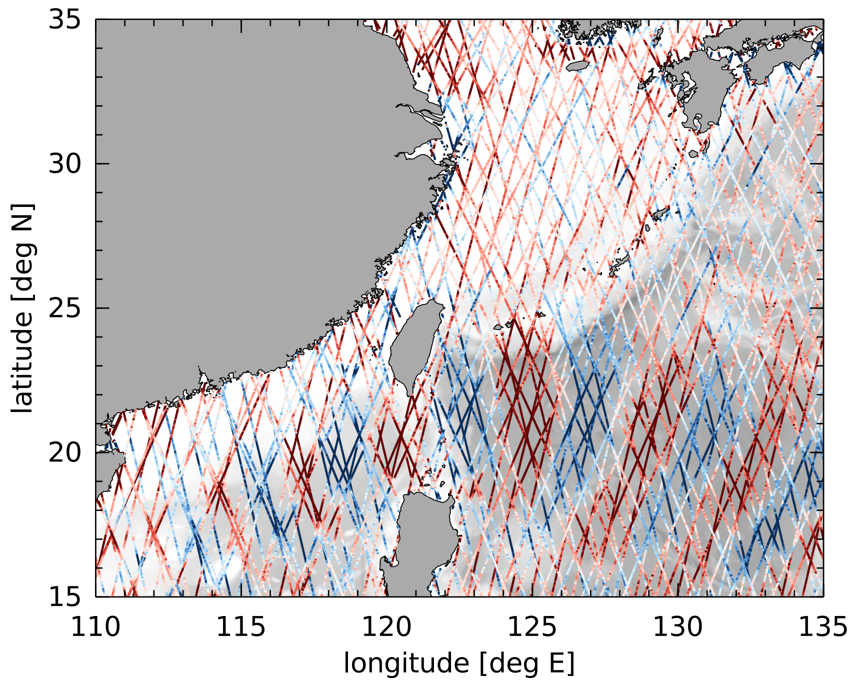

FIG. 11. In-phase component of K_1 tide, computed from collinear satellite altimeter data. The red-white-blue color range corresponds ± 2 cm range of tidal elevation. Background grayscale image displays the ocean topography. The baroclinic waves are largely confined to deep water and the spatial signal model does not capture the abrupt transition at the continental shelf break, e.g., near 125°E–24°N.